

Modeling swash-zone hydrodynamics and shear stresses on planar slopes using Reynolds-Averaged Navier–Stokes equations

Alec Torres-Freyermuth,¹ Jack A. Puleo,² and Dubravka Pokrajac³

Received 23 September 2011; revised 19 December 2012; accepted 21 December 2012; published 11 February 2013.

[1] A numerical model solving the Reynolds-Averaged Navier–Stokes equations, with a volume of fluid-tracking scheme and turbulence closure, is employed for estimating hydrodynamics in the swash zone. Model results for run-up distance, water depth, and near-bed velocity are highly correlated ($r^2 > 0.97$) with ensemble-averaged dam-break-driven swash data. Moreover, modeled bed shear stresses are within 20% of estimates derived from measured velocity profiles. Dam-break-driven swash simulations are conducted to determine the effect of foreshore characteristics (bed roughness and foreshore slope) on bore-induced swash-zone hydrodynamics and bed shear stresses. Numerical results revealed that the boundary layer vanishes during flow reversal, grows during the backwash, and becomes depth limited at the end of the swash cycle. In general, the uprush experiences larger shear stresses but for a shorter duration than the backwash. Some variability in this pattern is observed depending on the bed roughness, foreshore slope, and cross-slope location in the swash zone, implying that large spatial gradients in shear stresses can occur on the foreshore. The mean tangential force per unit area supplied to the bed is offshore directed for the simulated cases, with the exception of the mild-slope (1:25) cases, owing to the skewed nature of swash flows. The temporal evolution of the momentum balance inside the swash zone shows an important contribution to the total force from turbulence and advection at the early/final stage of the swash cycle, whereas the local acceleration does not appear to be a significant contribution.

Citation: Torres-Freyermuth, A., J. A. Puleo, and D. Pokrajac (2013), Modeling swash-zone hydrodynamics and shear stresses on planar slopes using Reynolds-Averaged Navier–Stokes equations, *J. Geophys. Res. Oceans*, 118, 1019–1033, doi:10.1002/jgrc.20074.

1. Introduction

[2] The foreshore, the region of the nearshore profile covered and uncovered by swash flows, undergoes bathymetric evolution that depends on gradients in sediment transport patterns driven by fluid processes including bed shear stresses. Many field and laboratory studies have investigated cross-shore swash-zone fluid velocities leading to the general consensus that, on steep beaches, peak uprush cross-shore velocity magnitudes tend to be nearly equivalent to [e.g., Cowen *et al.*, 2003; Masselink *et al.*, 2005; Puleo *et al.*, 2003] or greater than [e.g., Hughes *et al.*, 1997a; Masselink and Hughes, 1998; Hughes and Baldock, 2004] peak backwash cross-shore velocities, whereas the duration of backwash flow tends to exceed that of the uprush [e.g., Cowen *et al.*, 2003;

Hughes *et al.*, 1997b; Masselink and Hughes, 1998; Petti and Longo, 2001; Puleo *et al.*, 2000]. However, these findings need to be considered in a broad general context since natural swash is typically irregular such that individual swash events can display characteristics opposite to those mentioned above.

[3] In contrast to the abundant swash-zone velocity measurements in the literature, shear stress measurements are more scarce. Laboratory studies often estimate the bed shear stress utilizing knowledge of the velocity profile. Cox *et al.* [2000] obtained swash-zone velocity profiles over a fixed, roughened bed using a laser Doppler velocimeter. After fitting a log-law to the data, temporal variations in bed shear stresses from the swash zone driven by random waves were shown to be maximal when the measurement location was first wetted. Shear stresses decreased rapidly and became offshore directed at roughly 1/3 of the swash duration. Offshore-directed stresses peaked at one fourth the magnitude of onshore-directed stresses and were maximal as the location became unwetted. Cowen *et al.* [2003] obtained swash-zone velocity measurements using particle image velocimetry (PIV) directing the light sheet into the measurement region from underneath a planar sloping smooth glass beach. They estimated the bed shear stresses by fitting the velocity profile to a log-law and assuming a constant stress layer near the bed employing direct estimates of dissipation from velocity data and from a spectral estimation of the dissipation. Stress profiles from ensemble-averaged data driven by monochromatic waves indicated typically similar time histories for swash

¹Laboratorio de Ingeniería y Procesos Costeros, Instituto de Ingeniería, Universidad Nacional Autónoma de México, Sisal, Yucatán, México.

²Ocean Engineering Laboratory, Center for Applied Coastal Research, Department of Civil and Environmental Engineering, University of Delaware, Newark, Delaware, USA.

³School of Engineering, University of Aberdeen, King's College, Aberdeen, AB24 3UE, United Kingdom.

Corresponding author: Alec Torres-Freyermuth, Laboratorio de Ingeniería y Procesos Costeros, Instituto de Ingeniería, Universidad Nacional Autónoma de México, Sisal, Yucatán México. (atorresf@ii.unam.mx)

initiated by plunging and spilling waves. In both cases, peak onshore-directed stresses occurred just after the measurement region was wetted. Change in stress direction, presumably at the minimum in the stress history, occurred either at the mid duration point or slightly after unlike that found in the *Cox et al.* [2000] study. Backwash stresses were only marginally smaller than peak uprush stresses and were maximal as the measurement region became unwetted.

[4] *O'Donoghue et al.* [2010] reported high-resolution PIV measurements across the swash zone for a single dam-break-driven swash event. Velocity profiles at different cross-shore locations were used to infer the bed shear stresses by fitting a log profile for both smooth and rough beds. Consistent with *Cowen et al.* [2003] data, the peak uprush and backwash shear stress magnitudes are similar at many cross-shore locations inside the swash zone. *Barnes et al.* [2009] presented direct bed shear stress measurements for the same experimental conditions using a shear plate. The bed shear stress time series indicated a reduced peak backwash shear stress relative to that obtained from the velocity profile [*O'Donoghue et al.*, 2010]. The latter finding suggests that bed shear stress estimates based on log-law fitting of the velocity profile may not be reliable during the backwash or the velocity profile may have been under-resolved. In another study, *Sou et al.* [2010] measured the velocity field and turbulence structure under monochromatic waves using PIV. The temporal evolution of the turbulence over a wave cycle consists of the wave-breaking and shear-layered-generated turbulence during bore arrival, a decay stage near flow reversal, and bed-generated turbulence during the latter stage of the backwash phase. *Sumer et al.* [2011] investigated solitary wave evolution on both an impermeable (fixed) and sediment (movable) bed. Measured bed shear stress and vertical pressure gradients were employed from the two cases in order to qualitatively explain the bed morphology change.

[5] Obtaining the shear stress in field settings is more complicated because the bed is mobile and many of the laboratory procedures for obtaining highly resolved velocity profiles are not feasible. The general approach is to utilize a coarse representation of the velocity profile in an effort to estimate the shear stress [*Masselink et al.*, 2005; *Raubenheimer et al.*, 2004], incorporate horizontal and vertical velocity information into the estimate [*Aggaard and Hughes*, 2006], or utilize a quadratic drag law and an empirical friction coefficient [e.g., *Butt et al.*, 2005; *Masselink and Hughes*, 1998; *Puleo et al.*, 2000, among many others]. Recently, a high-resolution acoustic Doppler current profiler has been utilized to obtain swash-zone velocity profiles at millimeter resolution over the lower 10–30 mm of the water column [*Puleo et al.*, 2012]. Ensemble-averaged velocity profiles away from flow reversal were well represented by the log-law. Corresponding peak shear stresses were found to be larger during offshore-directed flow than onshore-directed flow (possibly due to aeration complicating measurements during the beginning stages of onshore-directed motion) and maintained a time history similar that reported by *O'Donoghue et al.* [2010].

[6] The only direct estimates of swash-zone shear stresses in the field, to our knowledge, were obtained using a hot film probe [*Conley and Griffin*, 2004]. The probe was mounted to a permeable brick that resembled the sediment characteristics of the field site where the study was undertaken. The peak

uprush shear stress was nearly double that during backwash, but backwash duration was approximately 1.5 times the uprush duration.

[7] Fluid velocities and shear stresses are both of paramount importance because their product is often used to describe sediment transport patterns through an energetics model [*Bagnold*, 1963; *Bowen*, 1980; *Bailard*, 1981] even though several studies suggest this model alone is inadequate for predicting swash-zone sediment transport [e.g., *Aggaard and Hughes*, 2006; *Butt et al.*, 2005; *Masselink and Puleo*, 2006]. However, shear stresses must play a major role in sediment mobilization. As mentioned previously, the general approach for estimating shear stress is to use a drag law formulation. Unfortunately, the embedded friction coefficients used have at least an order of magnitude range allowing for large variations in sediment transport predictions [*Conley and Griffin*, 2004; *Cowen et al.*, 2003; *Cox et al.*, 2000; *Hughes*, 1995; *Puleo and Holland*, 2001; *Raubenheimer et al.*, 2004]. The fact that little is known about swash-zone shear stresses stems from the extreme difficulties in obtaining laboratory or field measurements that are required to estimate their magnitude and temporal structure.

[8] Flow description in the swash zone also represents a challenging task for mathematical and numerical modelers. Specific difficulties arise in tracking the wet/dry interface and prescribing the correct forcing at the seaward boundary [*Brocchini and Baldock*, 2008; *Guard and Baldock*, 2007]. Some advances in the modeling of this region have been achieved using numerical implementations based on the Nonlinear Shallow Water Equations (NLSW) [*Hughes and Baldock*, 2004; *Kobayashi et al.*, 1989; *O'Donoghue et al.*, 2010; *Raubenheimer*, 2002]. Nevertheless, drawbacks of these models include the parameterization of energy losses through an empirical coefficient, no prediction of the vertical velocity, and the assumptions of hydrostatic pressure and depth uniformity of the velocity profile. Therefore, wave boundary layer modeling cannot be resolved directly with this approach. Some of these limitations have been overcome using either Eulerian [*Briganti et al.*, 2011] or Lagrangian [*Barnes and Baldock*, 2010] boundary layer models forced by depth-averaged velocities from the NLSW models. However, these models rely on the assumption that the velocity profile in the water column is logarithmic in the boundary layer and uniform above it. Moreover, they do not provide detailed information about turbulence, which should also affect sediment entrainment and transport. On the other hand, numerical models based on the Reynolds-Averaged Navier–Stokes (RANS) equations, while computationally expensive, provide an opportunity to overcome the aforementioned limitations and investigate the bore-induced, highly complex flow structure including turbulent boundary layer processes [e.g., *Zhang and Liu*, 2008; *Torres-Freyermuth and Hsu*, 2010].

[9] In this study, swash-zone bed shear stresses are simulated numerically using a two-dimensional (2D) Navier–Stokes model [*Lin and Liu*, 1998; *Losada et al.*, 2008; *Torres-Freyermuth and Hsu*, 2010]. The laboratory experiments employed for the model validation [*O'Donoghue et al.*, 2010] are briefly described in section 2. Then, the numerical model and the implementation of the simulated cases are presented in section 3. In section 4, the numerical model is validated and further employed, using different foreshore slopes and bed roughness, for a numerical investigation

of bed shear stresses and momentum balance induced by dam-break-driven swash. Concluding remarks are given in section 5.

2. Experimental Setup

[10] Novel experiments of dam-break-driven swash [O'Donoghue *et al.*, 2010, only an overview given here] provide a unique data set for the validation and calibration of numerical models of swash flow. The experiments were conducted in a 20 m long, 0.9 m high, and 0.45 m wide glass-sided flume (Figure 1a). The x - z axes have an origin at the still water level intersection and z is perpendicular to the bed. The dam-break rig consists of a water reservoir located at the offshore end of the flume fronted by a gate designed to be raised at high speed. The gate opening produces a bore that generates a swash event on the beach located at a distance (l_0) 4 m downstream. The resulting swash magnitude is similar to that of large swash events in the field [O'Donoghue *et al.*, 2010] but with perhaps a thinner swash lens owing to the limited amount of water in the reservoir. Two impermeable beach experiments using smooth and roughened 1:10 slopes were conducted. The reservoir length (l_T), reservoir water depth (h_T), and ambient water depth (h_0) were set at 1 m, 0.65 m, and 0.065 m, respectively. The smooth beach was composed of Perspex panels, whereas the roughened beach contained a layer of well-sorted, rounded pebbles (5 to 6 mm diameter) glued onto the impermeable beach slope. Water depth was measured at 100 Hz using 25 wave gauges across the swash zone. High-resolution velocity profiles were recorded at five cross-shore locations within the swash zone using PIV with a sampling frequency of 13 Hz. Ensemble-averaged water depth and velocity profiles at each location were obtained by O'Donoghue *et al.* [2010] from 50 different swash event realizations [O'Donoghue *et al.*, 2010, Figure 3]. Repeatability of the dam-break wave was demonstrated by O'Donoghue *et al.* [2010] with small variability being attributed to turbulence. For these experiments, O'Donoghue *et al.* [2010] calculated bed shear stresses based on the log-law fit of the velocity profiles at these five locations, and Barnes *et al.* [2009] measured the bed shear using a stress plate at

two of the locations and were corrected for pressure gradient caused by the surface elevation. Both studies were carried out at the same laboratory facility and under the same conditions, but at different times.

3. Numerical Model

3.1. Mathematical Formulation

[11] A minimum modeling approach to fully calculate non-linear wave propagation and wave-induced bottom boundary layer processes requires a depth- and phase-resolving model that solves the 2D RANS equations with a turbulence closure and a free-surface tracking scheme. Lin and Liu [1998] developed a model (COBRAS) that satisfies these constraints. The numerical model is based on an original version of a 2D fluid dynamics model developed at Los Alamos National Laboratory known as RIPPLE [Kothe *et al.*, 1991]. Full description of the model is provided by Kothe *et al.* [1991], Liu and Lin [1997], and Losada *et al.* [2008], and only a brief overview is given here. The model solves the 2D RANS equations for an incompressible fluid

$$\frac{\partial \langle u_i \rangle}{\partial x_i} = 0 \quad (1)$$

$$\frac{\partial \langle u_i \rangle}{\partial t} + \langle u_j \rangle \frac{\partial \langle u_i \rangle}{\partial x_j} = -\frac{1}{\rho} \frac{\partial \langle p \rangle}{\partial x_i} + g_i + \frac{1}{\rho} \frac{\partial \langle \tau_{ij} \rangle}{\partial x_j} - \frac{\partial \langle u'_i u'_j \rangle}{\partial x_j} \quad (2)$$

where t is time, x_i is the bed-parallel ($i=1$) and bed-orthogonal ($i=2$) coordinate, g_i is the gravitational acceleration component, u_i is the fluid velocity in direction x_i , ρ is the fluid density, p is the pressure, τ_{ij} is the shear stress, and angle brackets denote Reynolds-averaged quantities. The influence of turbulence fluctuations on the mean flow field is represented by the Reynolds stresses $\rho \langle u'_i u'_j \rangle$ that are approximated using a $k-\epsilon$ turbulence closure scheme. The governing equations for k (production of turbulent kinetic energy) and ϵ (energy dissipation rate) are derived from the Navier-Stokes equations, and higher-order correlations of turbulence fluctuations in the k and ϵ equations are replaced by closure conditions. The empirical coefficients of the ϵ equation were determined experimentally from stationary flows [Rodi, 1993; Wilcox, 2000]. A nonlinear algebraic Reynolds stress model is used to relate the Reynolds stress tensor and the strain rate of mean flow [Lin and Liu, 1998; Rodi, 1993]. The RANS equations are solved by the finite difference two-step projection method [Chorin, 1968]. In order to track free-surface locations, the volume of fluid (VOF) method is used [Hirt and Nichols, 1990], where the free surface is calculated by depth integration of the VOF value at the center of each cell. For more details, refer to Lin and Liu [1998] where model equations, coefficient values, and boundary and initial conditions of the original numerical code were introduced.

3.2. Numerical Implementation of the Simulated Cases

[12] The numerical implementation of the dam-break-driven swash experiment is straightforward using a standard reference frame for the model domain. However, the bottom boundary condition is not well posed under this situation owing to the required use of partial cells associated with the solid obstacle [see Kothe *et al.*, 1991]. Instead, sloping

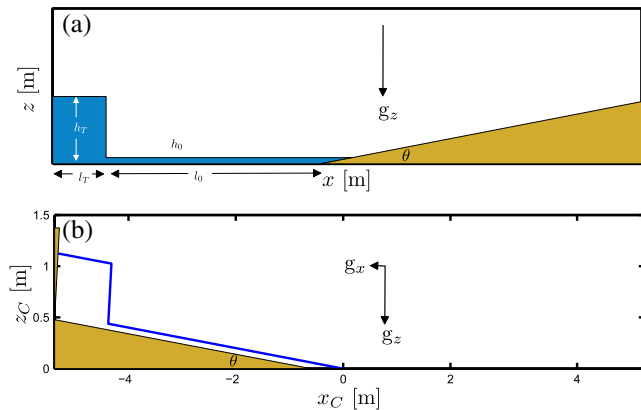


Figure 1. (a) Experimental setup of the dam-break-driven swash experiment of O'Donoghue *et al.* [2010]. The parameters are: $h_T=0.65$ m, $l_T=1.0$ m, $h_0=0.065$ m, $l_0=4.0$ m, and $\tan \theta=0.1$. (b) Numerical setup of (a) with the mesh oriented parallel to the foreshore slope.

bathymetry is accommodated by solving (1) and (2) in a model coordinate system that is bed parallel (x_C) and bed orthogonal (z_C) [e.g., *Puleo et al.*, 2007; *Zhang and Liu*, 2008], rather than cross shore (x) and vertical (z), as shown in Figure 1b. The rotated coordinate system allows an increased resolution within the wave boundary layer by decreasing the near-bed grid spacing and avoidance of possible spurious pressures [*Zhang and Liu*, 2008]. For the simulated cases the minimum cell size is $\Delta x_C = 5$ mm and $\Delta z_C = 3$ mm inside the swash zone. From 156 mm above the bed, grid spacing is more coarse ($\Delta z_C = 18$ mm) in order to decrease computational time. The model domain is changed, for computational efficiency, depending on the maximum runup (i.e., bed roughness) and beach geometry (i.e., slope). For instance, for the steep slope cases, the domain is 9 m long and 2 m high, whereas in the mild-slope cases, the domain is 14 m long and 1.3 high. The bottom boundary condition for a numerically roughened bed is imposed assuming a logarithmic law between the bottom of the domain and the first grid point above the bed [*Lin and Liu*, 1998]. It is noted that the requirement of a logarithmic law is not enforced for grid points higher in the domain with the velocity determined through solution of equations (1) and (2). The friction velocity, u_* , is calculated based on logarithmic velocity profile between the bottom and the half grid point above the bed

$$u_* = \frac{\kappa u(\Delta z_C/2)}{\ln\left[\frac{30\Delta z_C/2}{K_s}\right]} \quad (3)$$

where κ is the von Karman constant (0.4), and K_s is the apparent roughness. The roughness height, K_s , in boundary layer models is often parameterized as 1–2 grain diameters [*Justesen*, 1988]. However, this value can increase with increasing free-stream flow velocity/oscillatory periods and depending on the turbulence closure scheme employed [*Hsu et al.*, 2006]. For simplicity, we set K_s equal to $2D_{50}$ [*Hsu et al.*, 2006; *Justesen*, 1988] where D_{50} is the median grain diameter. Shear stresses, τ , are computed from

$$\tau = \rho(v + \nu_T) \left[\frac{\partial u}{\partial z_C} + \frac{\partial w}{\partial x_C} \right] \quad (4)$$

where u is the bed-parallel velocity, w is the bed-orthogonal velocity, and ν is the kinematic viscosity ($1.1 \times 10^{-6} \text{ m}^2 \text{ s}^{-1}$; water temperature = 17°C). The turbulent eddy viscosity, ν_T , is obtained from the $k - \epsilon$ turbulent closure solution as

$$\nu_T = C_\mu \frac{k^2}{\epsilon} \quad (5)$$

where $C_\mu = 0.09$ is a closure coefficient [*Wilcox*, 2000]. The bed shear stress is computed using equation (4) at the nearest grid point above the bed. As an initial condition, for all cases, the water surface is defined so it matches the reservoir length (l_T), reservoir water depth (h_T), and ambient water depth (h_0) of the experimental cases [*O'Donoghue et al.*, 2010] in a rotated reference frame. Furthermore, the beach is located at a distance (l_0) 4 m downstream of the dam for all cases, and hence the incoming bore at the beach toe is the same for all cases. The gate motion is not incorporated in the numerical model, but the water in the reservoir is released by gravity at the beginning of the simulation. The time step is automatically adjusted during the computation to satisfy the stability constraints (Courant number). The

computation times, for each simulation, on an Intel Xeon 2.53 GHz (6GB) computer range from approximately 4 to 8 h (Table 1).

[13] Different cases (Table 1) varying the foreshore characteristics are employed (section 4) in order to investigate hydrodynamics and bed shear stress variability across the swash zone. We focus on steep slopes where incident-bore-driven motions rather than infragravity waves are more often the dominant forcing mechanism inside the swash zone. The hydrodynamic forcing is set as constant for all simulations, whereas both the foreshore slope and bottom roughness are varied.

4. Model Results

4.1. Model Validation

[14] Although the RANS model has been widely validated within the surf zone on sandy [e.g., *Torres-Freyermuth et al.*, 2007, 2010] and gravel [e.g., *Lara et al.*, 2006; *Pedrozo-Acuna et al.*, 2010] beaches, less effort has been devoted to RANS model validation inside the swash zone [e.g., *Zhang and Liu*, 2008] partially owing to the lack of highly resolved velocities in this region. Experiments of dam-break-driven swash [i.e., *O'Donoghue et al.*, 2010] provide a suitable data set for model validation. Measured water depth, velocity, runup distance, and bed shear stresses, at different cross-shore locations, during the swash event are employed for the model-data comparison. Model output was recorded at 20 Hz and down-sampled to 13 Hz, when necessary, for comparison to laboratory data.

[15] The simulated CASES 7 and 15 correspond to the rough bed and smooth bed cases of *O'Donoghue et al.* [2010], respectively (see Table 1). Instantaneous water depths for the rough bed (CASE 7) for the model and data, at different stages of the swash duration, indicate good overall visual correspondence (Figure 2). The solid line corresponds to the model prediction and the open circles to the wave gauge measurements. Larger differences are observed during the bore arrival at the initial stage of the uprush (Figure 2a). This may be ascribed to possible effects of the gate motion on the bore generation that are not reproduced in the numerical model but may also be due to inadequate description of the turbulence in the bore. However, the larger

Table 1. Dam-break Simulated Cases

Case	Foreshore Slope	D_{50} [mm]	Computational Time [h]
CASE 1	1:25	10	≈8
CASE 2	1:15	10	≈8
CASE 3	1:10	10	≈8
CASE 4	1:5	10	≈5
CASE 5	1:25	5.5	≈8
CASE 6	1:15	5.5	≈8
CASE 7	1:10	5.5	≈7
CASE 8	1:5	5.5	≈5
CASE 9	1:25	0.5	≈8
CASE 10	1:15	0.5	≈8
CASE 11	1:10	0.5	≈6
CASE 12	1:5	0.5	≈6
CASE 13	1:25	0.2	≈8
CASE 14	1:15	0.2	≈8
CASE 15	1:10	0.2	≈7
CASE 16	1:5	0.2	≈4

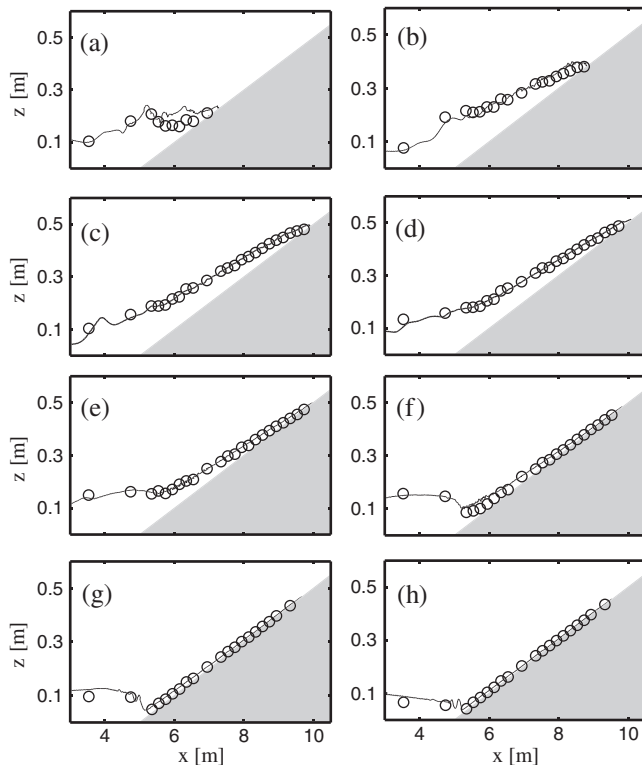


Figure 2. Measured (open circles) and predicted (solid line) profiles of ensemble-averaged water depth (CASE 7) during the (a–d) uprush and (e–h) backwash stages. (a) $t = 2.4$ s; (b) $t = 3.4$ s; (c) $t = 4.5$ s; (d) $t = 5.4$ s; (e) $t = 6.5$ s; (f) $t = 7.4$ s; (g) $t = 8.5$ s, and (h) $t = 9.4$ s.

elevation differences are not present for later times (Figures 2b–2f), and the model appears adept at quantifying the spatiotemporal variability in water depth for both uprush (Figures 2a–2d) and backwash (Figures 2e–2h). Direct correlation between model-derived and measured depths (a total of 1575 values) is $r^2 = 0.98$ significant at the 99% level. The least squares regression slope of 0.97 and intercept of 4.3×10^{-3} indicate little offset and essentially no gain between the modeled and measured water surface elevations.

[16] Model predictions of the run-up edge were estimated by identifying the most landward point whose water depth exceeded 4.5 mm for both smooth bed and rough bed simulations. It is important to point out that in the simulated cases, a thin layer of water remains on the beach surface during the backwash stage leading to our choice of 4.5 mm as a threshold depth value. This problem might be related to limitations of equation (3) to prescribe the bottom boundary condition for the thin-layer flow during the backwash. Notice that bed-parallel velocities are defined at the centers of the lateral faces (e.g., at height above the bed 1.5 mm, 4.5 mm, etc.), and hence the threshold used here corresponds to the location of the second velocity grid point. For each case, there is a steady increase in distance as a function of time until roughly $t = 6.0$ and $t = 5.3$ s, when the runup edge begins to recede (Figure 3). The runup for the smooth case (CASE 15) is nearly parabolic as expected for near frictionless ballistic motion [Kirkqz, 1981; Puleo and Holland, 2001; Shen and Meyer, 1963]. A departure from a parabolic trajectory is observed for the rough beach case (CASE 7). In situ runup distances

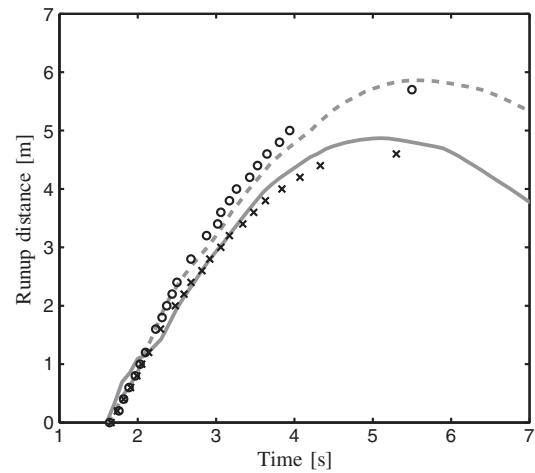


Figure 3. Measured (CASE 7: crosses, rough bed; CASE 15: circles, smooth bed) and predicted (CASE 7: solid line, rough bed; CASE 15: dashed line, smooth bed) runup distance as a function of time.

were identified using a runup wire located 3 mm above the bed but were not recorded for backwash. For the uprush portion, model predictions and runup measurements are highly correlated ($r^2 = 0.998$ and 0.993 for CASE 7 and CASE 15, respectively, significant at the 99% level). Root-mean-square errors (relative error during maximum uprush) for the two cases are 0.17 (4.23%) and 0.14 (1.22%), respectively.

[17] Model-data comparison of near-bed velocity measurements (CASE 7; $z_C \approx 4.5$ mm) at different cross-shore locations ($x_C = 0.5, 2.35, 3.0,$ and 3.5 m), indicate the model capability to predict swash-zone hydrodynamics (Figure 4). The measurement error of the PIV is not large ($10\text{--}20 \text{ mm s}^{-1}$), but there are two periods when the measurement conditions are difficult, one immediately after the bore arrival and another late into the backwash [O'Donoghue *et al.*, 2010]. Increased variability is probably caused by air entrainment at the beginning of the swash event and potential by cross-tank oscillations at the end of the event. The model is able to predict the timing of flow reversal, swash duration, and its trend as a function of onshore distance. The model is also capable of predicting the peak uprush velocity near bore arrival. It is important to point out that the difference in flow conditions between previous work [e.g., Cowen *et al.*, 2003; Sou *et al.*, 2010] and that of O'Donoghue *et al.* [2010] are related to scale effects (i.e., an order of magnitude increase in velocity) and the use of a rough bed for the O'Donoghue *et al.* [2010] study. Moreover, the dam break may produce a more turbulent swash event than the one owing to a typical breaking wave of similar height. Discrepancies during bore arrival can be partially ascribed to uncertainties of the PIV measurements, inaccuracies in the $k - \epsilon$ turbulence closure scheme, and limitations of the bottom boundary condition in the numerical model. In addition, the model has difficulty predicting the peak velocity and the temporal decrease in velocity during the end of the backwash when flows are extremely shallow. This is another period when experimental results are less certain [O'Donoghue *et al.*, 2010], but may also be due to specifying a constant value for computing the bottom boundary condition in the numerical model. Despite these differences, model velocity results are generally in a good

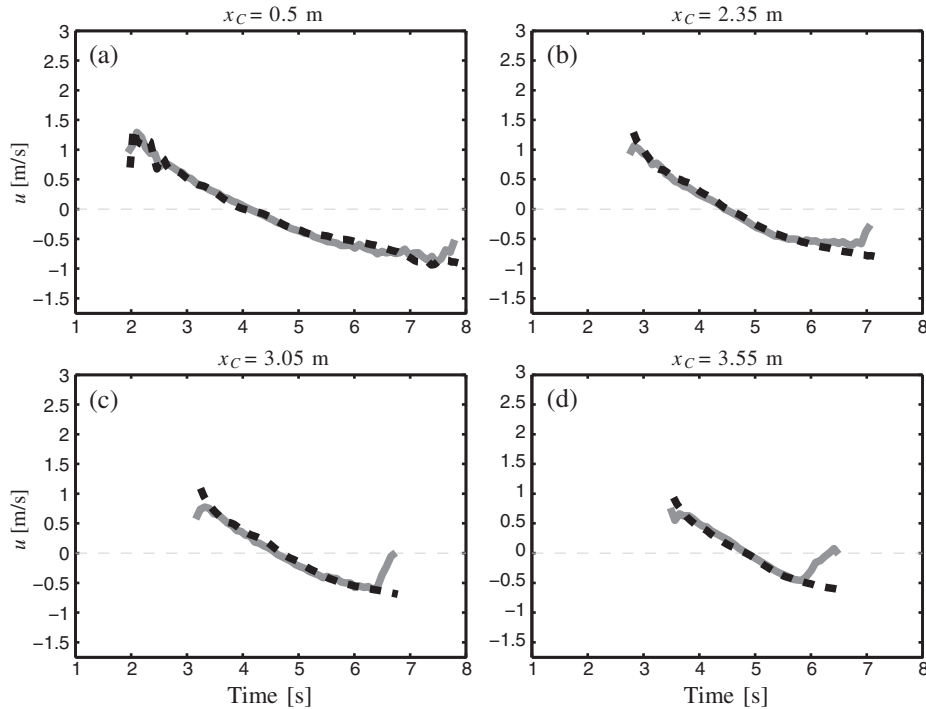


Figure 4. Model-data comparison of near-bed velocity (observations: light solid line; prediction: dark dashed line) at different cross-slope positions for CASE 7. The observations are based on the ensemble average of the measurements at (a) $x_C=0.5$ m and $z_C=4.8$ mm, (b) $x_C=2.35$ m and $z_C=4.6$ mm, (c) $x_C=3.05$ m and $z_C=5.2$ mm, and (d) $x_C=3.55$ m and $z_C=5.16$ mm. Model predictions are based on the model estimation at the nearest grid point where velocity is calculated (i.e., $z_C=4.5$ mm).

overall agreement with near-bed ($z_C=4.5$ mm) velocity measurements at all cross-slope locations shown in Figure 4. Moreover, correlation between simulated and the ensemble-averaged velocity measurements at the near-bed location is $r^2=0.97$ significant at 99% level.

[18] Simulated velocity profiles (solid curves) at different cross-slope locations ($x_C=0.5, 2.35, 3.0, \text{ and } 3.5$ m) during the swash event also indicate the model is capable of reproducing measurements (Figure 5; CASE 7). Ensemble average velocity (open circles) and turbulence contribution (± 1 standard deviation of the repetitions) are also represented in the figures. At times when the water surface is laterally tilted, the reflections of laser light affect the quality of PIV images, resulting in erroneous vectors that are discarded [O'Donoghue *et al.*, 2010]. The phase between the data and the model at each cross-slope location is the same. Near the still water intersection (Figure 5a), velocity magnitudes exceed 1.5 m s^{-1} during uprush and backwash. However, the larger velocities are observed and predicted closer to the bed during uprush than during backwash suggesting a temporal variability in boundary layer thickness. Peak uprush and backwash velocities decrease with distance up the beach slope, as expected (Figures 5b–5d). At $x_C=3.55$ m, the near-peak backwash velocity slightly exceeds 0.5 m s^{-1} , while the near-peak uprush velocity is 1.39 m s^{-1} . Some features such as the phase lead between the boundary layer flow and the free-stream velocity are captured by the model near the flow reversal phase (e.g., 5.4 s in Figure 5a; 5.6 s in Figure 5b; 5.9 s in Figures 5c–5d) when the boundary layer is not depth limited. The model captures the gross features of the velocity profiles at different spatiotemporal locations within the swash

zone. There are instances where the model is highly correlated to the ensemble-averaged data (e.g., $t=5.4, 6.3, \text{ and } 9$ s in Figure 5a), but other instances where the model produces poorer results (e.g., $t=4.9, 5.6, \text{ and } 5.9$ s in Figure 5d). Part of this discrepancy could be due to the larger variability during the initial stages of uprush as mentioned earlier but also slight timing variations between the model and actual conditions in terms of the wave-breaking event owing to gate motion effects on the laboratory experiments that are not accounted for in the model.

[19] The velocity measurements can be decomposed into the ensemble-averaged and turbulent fluctuation given the repeatability of the experiments by O'Donoghue *et al.* [2010], and hence the one component turbulence intensity can be obtained. On the other hand, the numerical model computes the turbulent kinetic energy directly by solving the $k-\epsilon$ equations. Figure 6 presents the model-data comparison of time series of turbulence intensity at different elevations (i.e., $z_C=0.45, 3.45, \text{ and } 11.25$ cm) for a given cross-shore location (i.e., $x_C=0.5$ m). The numerical model predicts the high turbulence level during bore arrival at all locations that is related to the bore-advected turbulence (Figures 6a–6c). The bed-generated turbulence during the backwash [Sou *et al.*, 2010] is also evident in the experimental data (bounds in Figure 5) and displays dependence with elevation from the bed, consistent with a developing boundary layer. For instance, an order of magnitude difference in the turbulence intensity magnitude at the different elevations occurs during the backwash phase (see Figures 6a and 6c). This latter feature is also well represented by the numerical model.

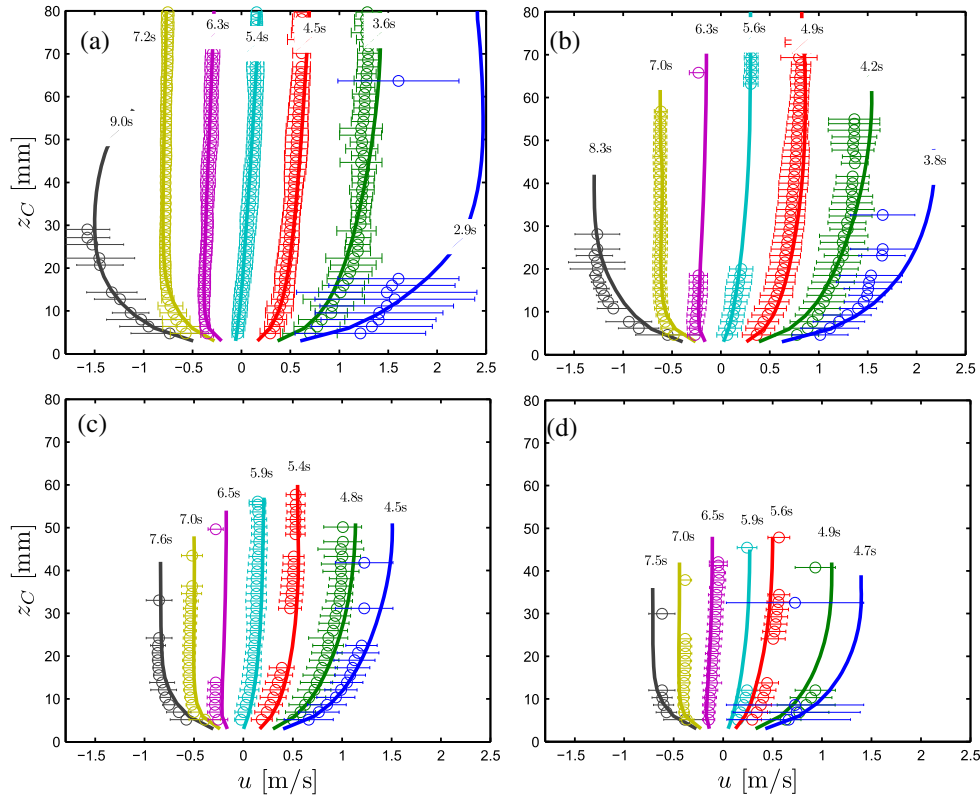


Figure 5. Model-data comparison of measured (circles) and predicted (solid lines) ensemble-averaged velocity profiles and turbulent velocity component (± 1 standard deviation) for CASE 7 at (a) $x_C=0.5$ m, (b) $x_C=2.35$ m, (c) $x_C=3.05$ m, and (d) $x_C=3.55$ m. The velocity profiles are plotted for the same relative swash phases at each location.

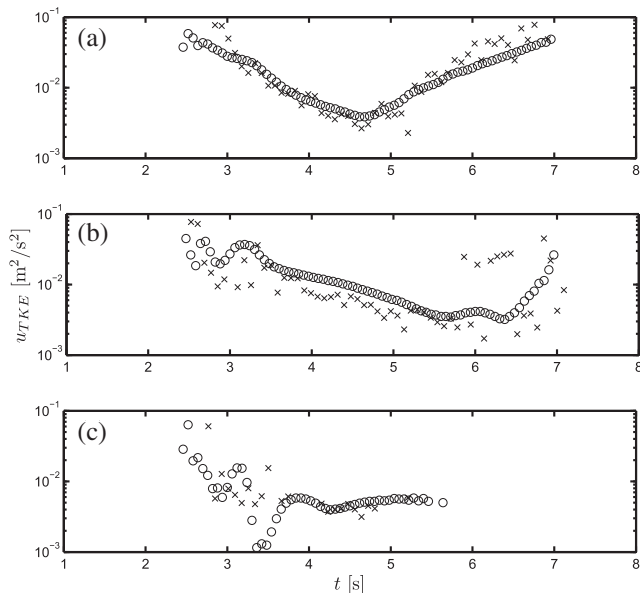


Figure 6. Time series of turbulence intensity (measured: crosses; predicted: open circles) for CASE 7 at $x_C=0.5$ m for (a) $z_C=4.5$ mm, (b) $z_C=34.5$ mm, and (c) $z_C=112.5$ mm.

[20] Finally, model prediction of bed shear stresses are compared against the shear stress estimates (see Figure 7) based on the velocity log-law fit of *O'Donoghue et al.*

[2010] (at $x_C=0.5$, $x_C=3.05$ m, and $x_C=3.55$ m) and the shear plate measurements of *Barnes et al.* [2009] (at $x_C=2.35$ and $x_C=3.05$ m). *Barnes et al.* [2009] and *O'Donoghue et al.* [2010] measurements were performed at the same laboratory facility and under the same conditions, but at different times. The relative error of observed [*O'Donoghue et al.*, 2010] and predicted maximum bed shear stress prediction during bore arrival is $\approx 20\%$ at the landward and seaward sections of the swash zone whereas a smaller error ($\approx 5\%$) is found at mid-swash locations. Numerical results and observations [*O'Donoghue et al.*, 2010] have similar errors ($\approx 40\%$ at $x_C \approx 2.0$ m and 10% at $x_C \approx 3.05$ m) with respect to the direct bed shear estimates [*Barnes et al.*, 2009] assuming the direct estimates are truly indicative of the actual bed stress. A comparison between the numerical model used in this study and the *Barnes et al.* [2009] observations (only obtained at $x_C \approx 2.35$ m and 3.05 m) suggests an improved agreement at the two locations for both uprush and backwash stages (Figure 7), especially at $x_C \approx 2.35$ m.

[21] The RANS model provides reliable predictions of the aforementioned hydrodynamic parameters inside the swash zone based on this test case. Model validation has motivated a more detailed investigation of swash-zone bed shear stress and hydrodynamics over different foreshore slopes.

4.2. Bed-parallel Velocity and Runup

[22] Interest in bed shear stresses implies the ability to compactly visualize the spatiotemporal nature of the stress

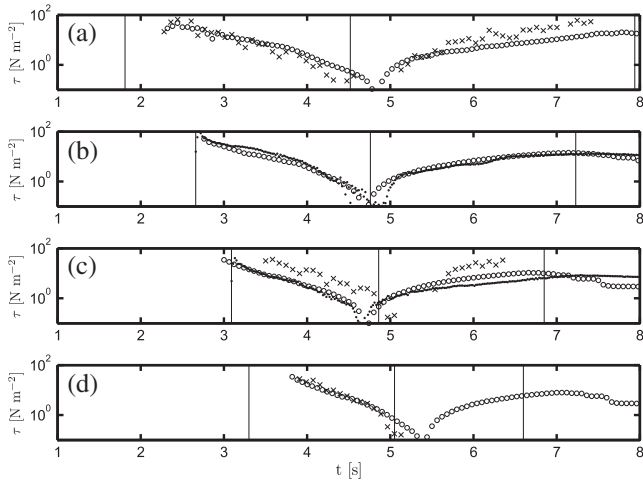


Figure 7. Time series of bed shear stress from log-fit (crosses) measured by *O'Donoghue et al.* [2010], shear plate bed shear stress (dots) measurements by *Barnes et al.* [2009], and model prediction for CASE 7 (open circles) at (a) $x_C=0.5$ m, (b) $x_C=2.35$ m, (c) $x_C=3.05$ m, and (d) $x_C=3.55$ m.

exerted near the bed. An appropriate means to achieve the visualization of numerical results is through a time stacking procedure. The time stack provides a simplistic means for nondimensionalizing swash event duration and extent for intercomparison. The temporal and lateral initiation point of the swash event begins where the zero velocity contour intersects an empty cell as denoted by the vertical gray and horizontal dashed gray lines in Figure 8. A swash event is defined to conclude when the backwash reaches the same bed-parallel location as that where the event was initiated. This definition is appropriate for dam-break-driven singular swash events, but not swash driven by irregular waves. The time between the swash initiation and termination points, as defined here, is deemed the event duration, D , and is used

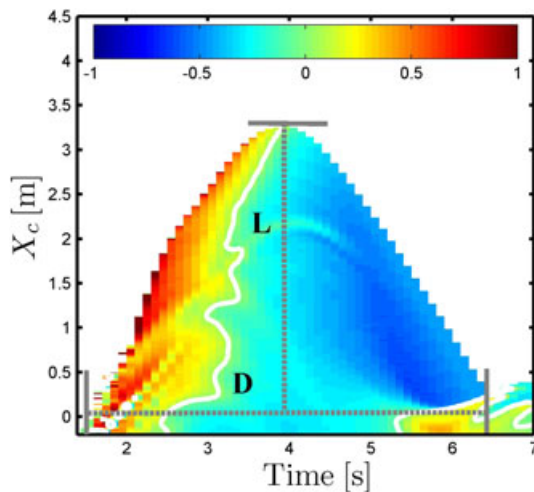


Figure 8. Bed-parallel cross-slope velocity time stack and normalized spatial (L) and temporal (D) swash parameters. The color bar indicates velocity [m s^{-1}] with positive velocities onshore directed. The white contour indicates zero velocity.

as a normalizing parameter. The bed-parallel runup distance, L , is defined as extending from the cross-slope position of swash initiation to the most landward location of swash motion (Figure 8). Using these normalizing parameters, new nondimensional swash coordinates are adopted. The nondimensional bed-parallel coordinate becomes

$$x' = \frac{x_{C,t} - x_{C,0}}{L} \quad (6)$$

where x_C and $x_{C,0}$ are the time-dependent and minimum cross-slope runup levels, respectively. Nondimensional time becomes

$$t' = \frac{t - t_{start}}{D} \quad (7)$$

where t is the time and t_{start} is the start time of the uprush.

[23] As an example, the time stack of bed-parallel velocity for CASE 8 at different water depths is presented in Figure 9. The beginning of the uprush is denoted by large onshore-directed velocities that quickly decrease in magnitude as a function of bed-parallel distance and time. As expected, the backwash begins from rest and increases in velocity as a function of downslope distance and time. The peak uprush/backwash velocity at a given cross-slope location increases with distance from the bed (i.e., Figures 9a-1, 9b-1, and 9c-1) and becomes more symmetric. In Figure 9 (left), the horizontal lines in the time stacks indicate the cross-slope position of swash initiation at the seaward (blue), middle (red), and landward (black) swash regions. Near-bed velocity magnitudes, inside the boundary layer, can reach 1 m s^{-1} at the beginning stage of the swash event (Figure 9a-2). On the other hand, near-surface velocity magnitude for this case and time is three times larger (Figure 9c-2). The bed-parallel velocity decreases in magnitude near the end of backwash at the mid- and near-surface elevations independent of cross-slope location (Figures 9b-2 and 9c-2) whereas this velocity decrease is not as evident at all cross-slope locations for the near-bed velocities (Figure 9a-2).

[24] Boundary layer streaming can play a significant role on net sediment transport in predominately sheet flow conditions [*Yu et al.*, 2010]. There are many ways to estimate the boundary layer thickness δ in the literature [e.g., *Nielsen*, 1992]. However, these estimates are typically used in flat plate boundary layer studies of steady flow. On the other hand, in the dam-break-driven swash, the flow is highly unsteady and nonuniform, where at times, there is no clearly identifiable free-stream velocity. Hence, it is difficult to apply some standard criterion of defining the boundary layer thickness based on the free-stream velocity information. We assume that the velocity profile satisfies the logarithmic law, and the elevation from the logarithmic fit to the n th point velocity measurements above the bed, where the correlation coefficient between measured and fitted velocities is ≥ 0.95 , is taken as an indicator of the boundary layer thickness. During some phases of the swash flow, the boundary layer spreads throughout the whole water depth and hence can be considered as depth limited. Figure 10 shows the observed and simulated boundary layer thickness δ with respect to time at $x_C = 0.5$ m. The instantaneous velocity profiles at selected locations are also shown in the upper right. In Figure 10, the boundary layer thickness based on our definition was presented for both uprush and backwash phases of swash, to be consistent with *Barnes and Baldock* [2010]. However,

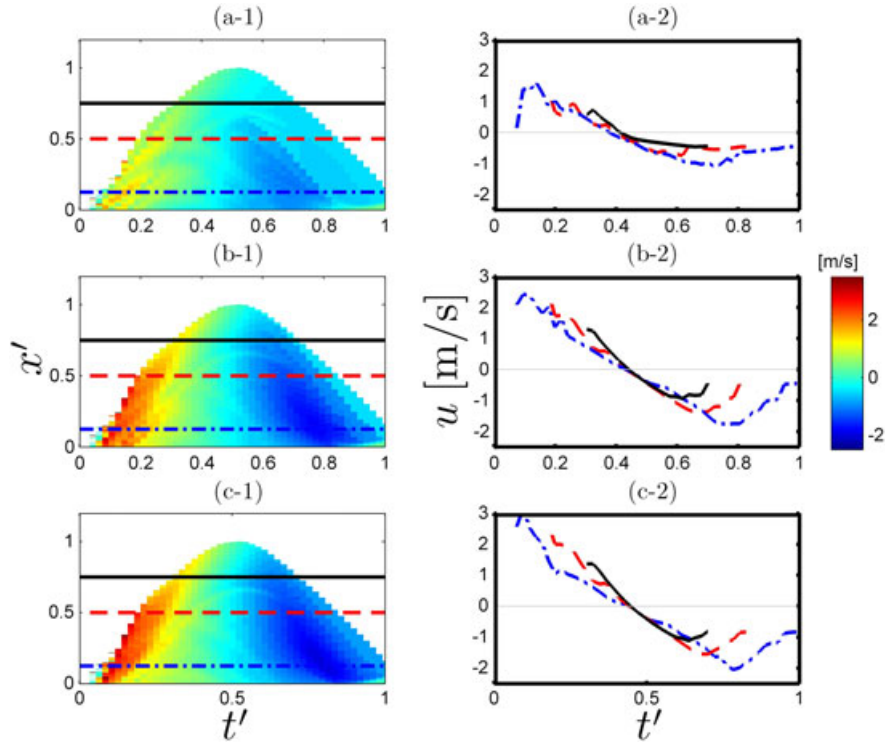


Figure 9. Bed-parallel, cross-slope velocity time stack of CASE 8 extracted from the (a-1) near-bed, (b-1) mid-depth, and (c-1) near-surface water depth. The corresponding time series at the seaward (blue dashed-dotted line), middle (red dashed line), and landward (black solid line) swash regions are shown in the right panels. The t' represent the nondimensional normalized swash period.

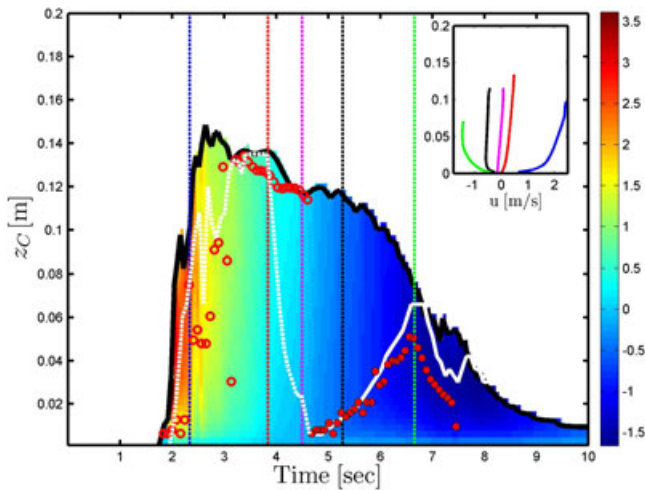


Figure 10. Water depth (black line), cross-slope velocity, and boundary layer thickness evolution based on the logarithmic boundary layer assumption (modeled: white line; observed: red circles) during the swash event at $x_c = 0.5$ m (CASE 7). During the uprush (model: dashed line; data: open circles), the wave boundary layer estimation using the logarithmic assumption may not be appropriate due to horizontal fluid straining owing to bore inertia. The vertical dashed lines correspond to simulated instantaneous velocity profiles shown in the upper-right figure. The bed-parallel velocity [m s^{-1}] is represented by the color contours. Positive velocities are onshore directed.

we differentiate the uprush phase as a dashed line because even though the flow may have a logarithmic profile, it may not result from bed shear stresses being transferred vertically via turbulent diffusion. Rather, bore arrival may alter the velocity profile through horizontal straining of the fluid elements. This effect may be evidenced by the spatial gradients in fluid vorticity (e.g., Yeh [1991]; Sou and Yeh [2011] and model predictions (not shown)). Thus, the reader should interpret the dashed boundary layer height in Figure 10 with caution as the boundary layer may not become depth limited during the uprush in the classic sense of logarithmic boundary layer. Through flow reversal δ vanishes (Figure 10 and Barnes and Baldock [2010]), grows during the backwash, and becomes depth limited at the end of the swash cycle.

[25] The runup distance (L) and swash duration (D) are calculated for all simulated cases (Table 2). The runup distance and swash duration are larger on the milder foreshore as expected. For the cases with the same foreshore slope, runup distance increases with decreasing bed roughness (e.g., CASES 1, 6, 10, and 14 from Table 2). The swash duration has a similar trend except for steeper slopes with smaller grain sizes where the durations become approximately equal (e.g., CASES 4, 8, 12, and 16). There is a general increase in the ratio L/D for a constant slope as the grain size decreases. The ratios between the uprush and backwash durations at different (normalized) cross-slope locations generally increase in the landward direction (Figures 11a and 11b). For a constant foreshore slope of 1:10, D_{ur}/D_{bw} (uprush duration/backwash duration) increases with decreasing bed roughness

Table 2. Spatial and Temporal Characterization of Swash Events

Case	L [m]	D [s]	L/D [ms^{-1}]
CASE 1	6.39	16	0.399
CASE 2	5.20	12.5	0.416
CASE 3	4.51	9.5	0.475
CASE 4	2.98	5.0	0.596
CASE 5	7.27	16	0.454
CASE 6	5.38	12.1	0.445
CASE 7	4.87	9.1	0.535
CASE 8	3.30	4.9	0.638
CASE 9	7.48	14.3	0.523
CASE 10	6.91	11.0	0.628
CASE 11	5.60	9.0	0.622
CASE 12	3.45	4.4	0.784
CASE 13	8.0	14.2	0.563
CASE 14	6.13	10.3	0.595
CASE 15	5.78	9.0	0.642
CASE 16	3.57	4.4	0.811

across the swash zone. In these instances, D_{ur}/D_{bw} is always less than 1 except for the smallest roughness case at the most landward swash location. On the other hand, altering the fore-shore slope, keeping constant the bed roughness (Figure 11b), affects the ratio D_{ur}/D_{bw} more at the seaward and very landward edges of the swash zone than in the mid-swash locations. Under constant roughness conditions, D_{ur}/D_{bw} is nearly always 1 for the steepest slope (CASE 12, 1:5) and less than 1 for other slopes (CASE 9, 1:25, and CASE 11, 1:10) except at the most landward swash location.

4.3. Spatial and Temporal Evolution of Swash-zone Bed Shear Stress

[26] Bed shear stresses are calculated in the model using equation (4) in order to generate shear stress time stacks.

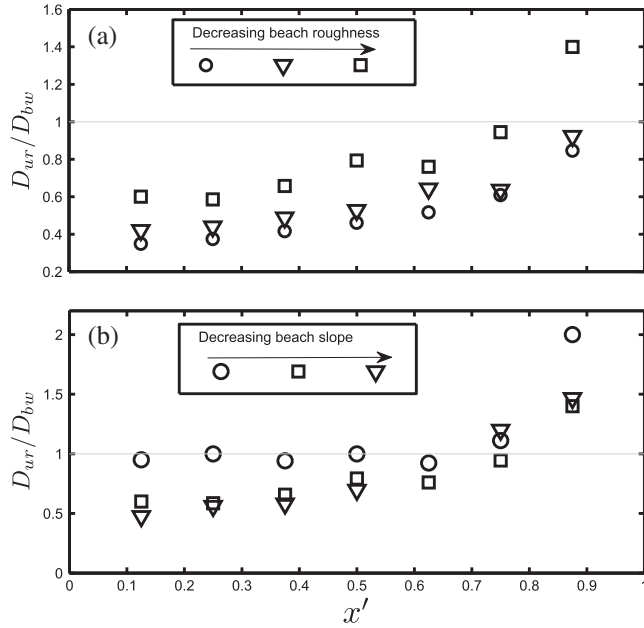


Figure 11. The ratios between the uprush and backwash duration, D_{ur}/D_{bw} , at different (normalized) cross-slope swash locations as a function of (a) bed roughness (CASE 3: circles; CASE 7: triangles; CASE 11: squares) and (b) beach slope (CASE 9: triangles; CASE 11: squares; CASE 12: circles).

The bed shear stress time stack for CASE 7 is shown in Figure 12 (upper panel), where bed shear stress is positive when the force acting on the bed is in the shoreward direction and the force acting on the fluid across the grain/fluid interface is in the seaward direction. Narrow regions of high onshore-directed stress are observed to occur followed by a broad region of smaller magnitude offshore-directed stress provided by skewed motion in the swash zone. This shape results from the larger shear stresses being located near the leading edge as opposed to within the swash interior. Shear stress magnitudes at a given cross-slope location decrease during uprush and increase during only a portion of the backwash. The maximum backwash shear stress magnitude occurs between $t' = 0.5$ and 0.7 before decreasing rather than continuing to increase until backwash termination. If sediment mobilization is related to shear stresses, then these large values should be expected to cause peaks in the amount of sediment in motion. Furthermore, since the shear stress decays fairly rapidly away from these regions, it may be suspected that this potential region of sediment mobilization is responsible for a disproportionate amount of the overall sediment motion in the swash zone pointing to the potential for sediment advection as a major contributor to the overall sediment transport budget in the seaward edge of the swash zone [Jackson *et al.*, 2004].

[27] One benefit of having high-resolution model information is the ability to extract shear stress time series by taking slices from the time stack matrix. Here, time series have been extracted at the three corresponding horizontal lines shown in Figure 12. Bed shear stress time series (Figure 12, lower panel) show a decrease of the peak magnitude in the landward direction from nearly 40 N m^{-2} to 25 N m^{-2} . Peak backwash stresses also vary but from about -20 N m^{-2} to -2 N m^{-2} . There

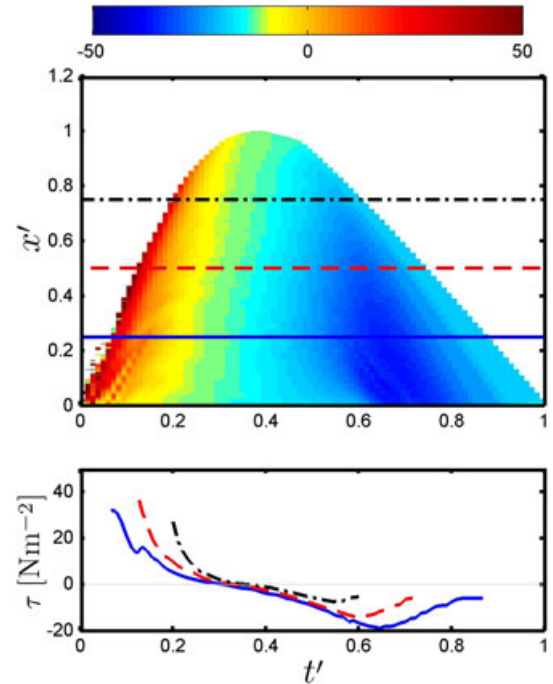


Figure 12. Bed shear stress time stack (N m^{-2} ; upper panel) and corresponding time series (lower panel) at seaward (blue line), middle (red dashed line), and landward (black dashed-dotted line) swash locations for CASE 7.

are obvious cross-slope gradients in shear stress from about $t' = 0.1$ to 0.25 during uprush and $t' = 0.5$ to 0.8 in the backwash.

[28] Figure 13 shows the evolution of the peak uprush and peak backwash shear stress as a function of cross-slope distance for cases with varying bed slope (CASES 6, 7, and 8, holding the grain roughness constant at 5.5 mm) and varying bed roughness (CASES 2, 6, and 14, holding the foreshore slope constant at $1:15$), respectively. The curves have been smoothed, with a tapered 50-point running average filter to reduce some of the singular spikes arising from cross-shore variability in peak stress largely owing to the turbulent nature of the dam-break bore. The maximum uprush bed shear stress is located in the seaward swash region (here defined as $x' < 1/4$) for most cases, consistent with *Barnes et al.* [2009]. However, the location varies slightly, depending on beach slope and bed roughness. The maximum backwash shear stress magnitude also occurs in the seaward swash region, but an obvious peak may not exist. In general, peak shear stress magnitude decreases roughly linearly as a function of x' for uprush and backwash. The increase in bed slope from $1:15$ (CASE 6) to either $1:10$ (CASE 7) or $1:5$ (CASE 8) results in the landward displacement of this maximum within the seaward swash region (Figure 13a). For the steeper beaches (CASES 7 and 8), there is a second local maximum in the landward swash region. This could be related to the vertical motion induced by the bore impingement on the slope. Unlike the uprush, the cross-slope distribution of peak backwash stresses is smooth, likely owing to a lack of surface-generated turbulence. For the milder beach slopes (CASE 6 and CASE 7), backwash stresses are weak with magnitudes never exceeding 20 N m^{-2} (Figure 13a).

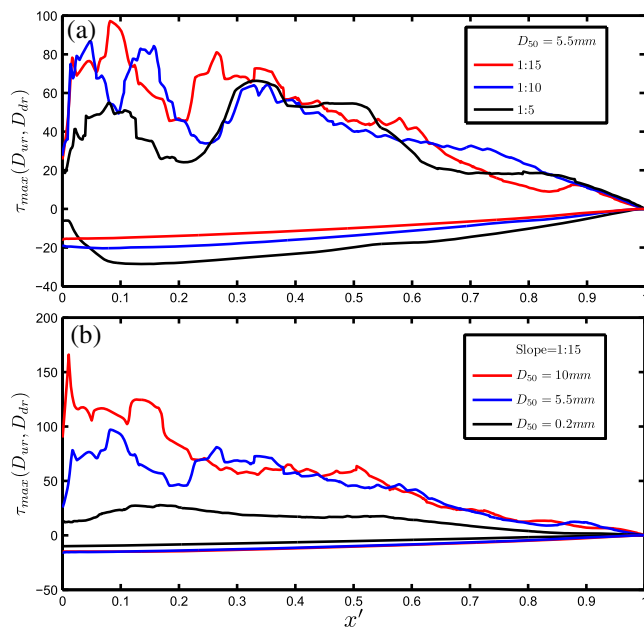


Figure 13. Peak uprush (positive values) and peak backwash (negative values) bed shear stress across the swash zone. (a) Effect of varying foreshore slope (CASE 6: red solid line; CASE 7: blue solid line; CASE 8: black solid line) and (b) bed roughness (CASE 2: red solid line; CASE 6: blue solid line; CASE 14: black solid line).

[29] Cross-slope variability in shear stress shows similar trends when the foreshore slope is held constant ($1:15$) and the roughness is altered (Figure 13b). However, the secondary local maximum in uprush peak shear stress is not as pronounced, and there is a clearer trend of the uprush peak shifting landward with increasing grain size. In general, peak uprush shear stress magnitudes exceed those in the backwash by a factor of 2–5 consistent with laboratory observations by *Barnes et al.* [2009].

[30] Mean stresses at discrete (normalized) swash locations (e.g., $\langle \tau'_{1/8} \rangle$) at the location $1/8$ of D from the swash initiation point) are obtained from the time stack by summing over rows of the matrix and dividing by the number of points where data exist. The results are summarized in Table 3 for all simulated cases. In general, the mean stress is negative (offshore directed) in the seaward swash region and increases landward reaching positive values in the landward swash region. Mild-slope small-roughness foreshores (i.e., CASE 14) have positive mean shear stress values across the mid- and landward swash regions. Similarly, the overall mean stress over rows and columns of the entire event $\langle \tau \rangle$ represents an average tangential force per unit area supplied to the foreshore during the entire swash event. For the simulated cases, the overall mean shear stress supplied to the bed is offshore directed for all cases except for the milder-slope foreshore ($1:25$). One explanation is that the larger-short duration shear stress spike during uprush is not able to compensate for the smaller but longer-duration backwash shear stresses. The magnitude shows a dependence with both slope and bed roughness. Increasing beach slope and bed roughness enhance the offshore-directed overall mean stress magnitude. Thus, maximum offshore overall mean shear stresses occurred for CASE 4.

4.4. Estimated Friction Coefficients From the Drag Law Formulation

[31] Estimates of bed shear stresses in a boundary layer can be obtained using several different methods. In the previous section, bed shear stresses were estimated via near-bed velocity gradients. Another method is to utilize the common quadratic parameterization for the bed shear stress

$$\tau = \frac{1}{2} \rho f u^2 \quad (8)$$

where f is an empirical friction coefficient. Normally, values for u in this formulation are taken from a vertical location where a measurement happens to be made irrespective of its location with respect to the boundary layer. This is often necessary because (1) the boundary layer in the swash zone varies over the swash event (see Figure 10) sometimes being depth limited by the free surface (i.e., backwash) and (2) current meter deployment in the laboratory and field normally occurs at one or only several vertical locations, with placement typically close to the bed. Utilizing equation (8) to determine τ requires specifying f , normally based on the estimated bed roughness. Formulas do exist for estimating f on smooth slopes for laminar flow and have been estimated by experimentation as a function of Reynolds number (see short overview by *Nielsen* [1992]). Here, we assume that equations (4) and (8) are equivalent and solve for f . In this manner, the friction coefficient can be determined using cross-slope velocities from various vertical locations. We note that nearly all prior studies

Table 3. Mean and Overall Mean Bed Shear Stress (N m^{-2}) Supplied to the Foreshore

Case	$\langle \tau'_{.1/8} \rangle$	$\langle \tau'_{.2/8} \rangle$	$\langle \tau'_{.3/8} \rangle$	$\langle \tau'_{.4/8} \rangle$	$\langle \tau'_{.5/8} \rangle$	$\langle \tau'_{.6/8} \rangle$	$\langle \tau'_{.7/8} \rangle$	$\langle \tau \rangle$
CASE 1	-0.778	-0.623	0.463	0.443	0.196	0.438	0.746	0.047
CASE 2	-2.108	-1.929	-0.602	0.740	0.987	0.173	0.173	-0.637
CASE 3	-3.741	-1.086	-2.477	-2.076	-0.79	0.329	0.776	-1.431
CASE 4	-5.300	-4.888	-3.900	-3.691	-1.429	-1.550	-0.386	-2.253
CASE 5	-1.099	-0.398	0.057	0.082	0.360	0.184	0.581	-0.082
CASE 6	-1.636	-0.881	-1.214	-0.492	-0.011	0.164	0.284	-0.556
CASE 7	-4.037	-3.555	-1.979	-1.304	-0.232	0.219	0.919	-1.372
CASE 8	-3.093	-5.830	-3.597	-0.528	-2.146	-2.005	1.654	-2.241
CASE 9	-0.556	0.435	0.249	0.405	0.452	0.424	0.147	0.151
CASE 10	-1.360	-0.634	0.069	0.203	0.155	0.377	0.306	-0.206
CASE 11	-2.250	-1.708	-1.107	-0.072	-0.038	0.222	0.600	-0.672
CASE 12	-1.618	-0.968	-0.641	-0.286	-0.173	0.380	0.962	-0.271
CASE 13	-0.577	0.056	0.111	0.221	0.248	0.262	0.138	0.012
CASE 14	-1.199	-0.822	-0.253	0.373	0.449	0.424	0.417	-0.099
CASE 15	-1.919	-1.043	-0.697	-0.468	-0.007	0.181	0.312	-0.593
CASE 16	-1.333	-0.076	-0.179	0.062	0.084	-0.080	0.831	-0.123

of swash-zone bed shear stress or sediment transport would use the velocity from said current meter independent of its relative location within the boundary layer. Therefore, friction coefficients are estimated using bed-parallel fluid velocities from just above the bed ($1/8h$), the instantaneous mid-water column ($1/2h$), just below the instantaneous free surface ($3/4h$), the depth-average velocity, and at the grid point closest to the lowest elevation a typical current meter could be deployed (i.e., $z_C = 10.5 \text{ mm}$). Friction coefficient time series from the landward ($x' = 7/8$) and middle swash regions ($x' = 1/2$) illustrate the intra-swash variability of f (Figures 14a and 14b). The friction coefficient increases at the very beginning of uprush followed by a slight decay. As the velocity slows, the friction coefficient again increases slightly to drastically near flow reversal. At the start of backwash, the f values are still large and decrease for a portion of the backwash duration before

increasing again as flow velocities decrease. Friction coefficients tend to be slightly larger during uprush than backwash with the largest values occurring near flow reversal. The shapes of the friction curves simulated in the present work are similar to those estimated by Cowen *et al.* [2003] from velocity measurements over a smooth glass beach, but the overall magnitudes are somewhat smaller. Friction estimates based on near-bed velocity result in an order of magnitude difference with respect to depth-average, mid-water depth, and near-surface velocity. Instantaneous uprush friction coefficient estimates using velocities from these other locations range from 1×10^{-2} to 1×10^{-1} for CASE 7 depending on the vertical and cross-shore location where velocity is extracted. During uprush, f determined using the depth-averaged velocity is roughly twice f determined using the near-surface, mid-depth, or velocity from a fixed elevation. The flow resistance for transitional and fully rough flow in an open channel can be given by [Yen, 2002],

$$f = \left[-\log_{10} \left(\frac{K_s}{14.8h} \right) + \frac{5.76}{(4Re)^{0.9}} \right]^{-2} \quad (9)$$

where $Re = u_d h \nu$ is the Reynolds number calculated using depth-averaged velocity, u_d , and water depth, h . Flow resistance results obtained with equation (9) are shown in Figure 14 (squares) for the backwash phase. Friction coefficients agree closely with those estimated using equations (4) and (8). The similarity between the two values suggests the potential application of equation (9) in depth-averaged models for backwash flow.

[32] Mean uprush and backwash friction coefficients for all cases using the depth-averaged velocity are summarized in Table 4. Only, the f values when $Re > 1000$ were considered for averaging. Using this restriction removes the large and unrealistic friction values near flow reversal. Mean friction coefficients range from 3×10^{-3} to 5×10^{-1} , with the lowest mean values during the backwash. The friction coefficient does not show a clear trend with respect to cross-slope location (consistent with Barnes *et al.* [2009] observations). However, the maximum of the mean f values, for the larger grain sizes (CASE 1–8), are observed at the seaward and landward swash regions for the backwash and uprush, respectively. These cases present similar values during both the uprush and backwash phase. On the other hand, for small grain size (CASE 9–16), the mean uprush friction coefficient across the swash zone is an order of magnitude larger than the mean

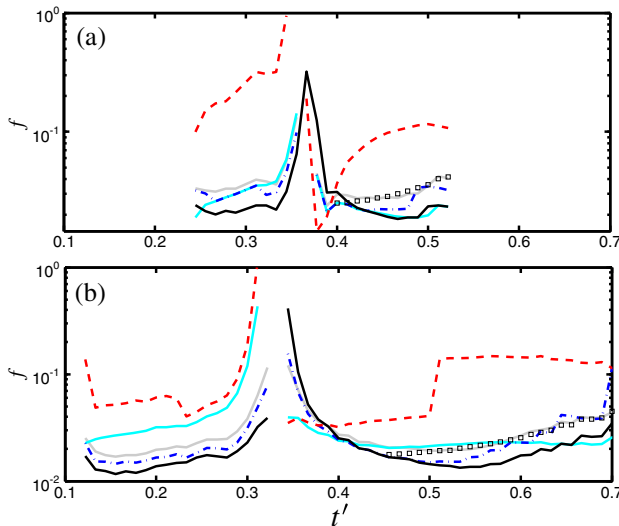


Figure 14. Friction coefficient time series at (a) landward ($x' = 7/8$) and (b) middle ($x' = 1/2$) swash-zone regions. The friction coefficients are calculated using instantaneous near-bed (red), mid-depth (blue), near-surface (dark solid line), depth-averaged (light solid line), and fixed-location ($z_C = 10.5 \text{ mm}$; cyan) cross-slope velocity in (9). Flow resistance for transitional and fully rough flow in an open channel, with the same characteristics, is denoted by pluses.

Table 4. Mean (a) Uprush and (b) Backwash Friction Coefficients Computed from Depth-averaged Velocity for $Re > 1000$

Case	$\langle f'_{t,1/8} \rangle$	$\langle f'_{t,2/8} \rangle$	$\langle f'_{t,3/8} \rangle$	$\langle f'_{t,4/8} \rangle$	$\langle f'_{t,5/8} \rangle$	$\langle f'_{t,6/8} \rangle$	$\langle f'_{t,7/8} \rangle$
(a) Uprush							
CASE 1	0.026	0.037	0.091	0.087	0.090	0.052	0.060
CASE 2	0.025	0.024	0.049	0.042	0.078	0.049	0.055
CASE 3	0.020	0.025	0.025	0.066	0.062	0.056	0.069
CASE 4	0.016	0.017	0.019	0.020	0.024	0.039	0.129
CASE 5	0.033	0.027	0.045	0.095	0.051	0.048	0.042
CASE 6	0.022	0.024	0.056	0.061	0.069	0.049	0.049
CASE 7	0.021	0.023	0.021	0.029	0.033	0.037	0.046
CASE 8	0.018	0.045	0.021	0.026	0.046	0.060	0.125
CASE 9	0.014	0.058	0.018	0.036	0.027	0.022	0.020
CASE 10	0.103	0.028	0.055	0.043	0.019	0.042	0.025
CASE 11	0.034	0.028	0.054	0.044	0.025	0.104	0.030
CASE 12	0.103	0.053	0.040	0.042	0.034	0.094	0.065
CASE 13	0.020	0.062	0.015	0.015	0.020	0.020	0.015
CASE 14	0.064	0.023	0.052	0.016	0.027	0.018	0.024
CASE 16	0.058	0.012	0.017	0.067	0.047	0.025	0.022
CASE 16	0.081	0.029	0.356	0.045	0.099	0.088	0.035
(b) Backwash							
CASE 1	0.062	0.050	0.045	0.047	0.049	0.055	0.056
CASE 2	0.076	0.054	0.070	0.052	0.059	0.061	0.063
CASE 3	0.076	0.066	0.068	0.053	0.061	0.069	0.065
CASE 4	0.245	0.868	0.125	0.372	0.060	0.090	0.060
CASE 5	0.028	0.055	0.028	0.029	0.030	0.030	0.029
CASE 6	0.039	0.034	0.034	0.031	0.031	0.033	0.031
CASE 7	0.053	0.033	0.058	0.033	0.030	0.032	0.031
CASE 8	0.162	0.034	0.041	0.043	0.271	0.033	0.032
CASE 9	0.009	0.008	0.009	0.008	0.008	0.008	0.005
CASE 10	0.009	0.009	0.009	0.008	0.008	0.008	0.007
CASE 11	0.009	0.008	0.008	0.008	0.008	0.008	0.006
CASE 12	0.008	0.008	0.008	0.008	0.008	0.007	0.005
CASE 13	0.006	0.007	0.007	0.006	0.006	0.005	0.004
CASE 14	0.006	0.006	0.006	0.006	0.006	0.005	0.004
CASE 15	0.006	0.006	0.006	0.006	0.006	0.005	0.004
CASE 16	0.006	0.006	0.006	0.006	0.005	0.005	0.003

backwash friction coefficient. The latter may be explained by the smaller bed-generated turbulence for these cases. Estimates confirm the expected trend for increased friction with grain size regardless of foreshore slope. In general, friction coefficient estimates of CASE 7 are within the values reported previously for the same case [Barnes *et al.*, 2009; O'Donoghue *et al.*, 2010]. Differences can possibly be attributed to the method they used to estimate f , namely a different method for estimating the bed-parallel velocity and the bed shear stress compared to this study.

term is often considered as a proxy for pressure gradients [Drake and Calantoni, 2001]. However, observations [e.g., Baldock and Hughes, 2006; Pedrozo-Acuna *et al.*, 2011] and numerical studies [e.g., Puleo *et al.*, 2007; Pedrozo-Acuna *et al.*, 2010] have suggested poor correlation between local acceleration and pressure gradients inside the swash and surf zones. We extend the previous work by Puleo *et al.* [2007] in order to investigate the role of all terms in the along-slope momentum RANS equation given by,

$$\underbrace{-\frac{1}{\langle \rho \rangle} \frac{\partial \langle p \rangle}{\partial x_C}}_I + g_x = \underbrace{\frac{\partial \langle u \rangle}{\partial t}}_{III} + \underbrace{\langle u \rangle \frac{\partial \langle u \rangle}{\partial x_C} + \langle w \rangle \frac{\partial \langle u \rangle}{\partial z_C}}_{IV} - \underbrace{\frac{1}{\langle \rho \rangle} \left(\frac{\partial \langle \tau_{xx} \rangle}{\partial x_C} + \frac{\partial \langle \tau_{xz} \rangle}{\partial z_C} \right)}_V \quad (10)$$

4.5. Momentum Balance in the Swash Zone

[33] The along-slope momentum equation is employed to investigate the role of advection and turbulence inside the swash zone. The pressure gradient and the downslope gravity terms in equation (2) represent the total force supplied to a unit mass of water that is important for sediment mobilization and transport [e.g., Madsen, 1974; Sleath, 1999; Foster *et al.*, 2006]. The local acceleration

[34] The dam-break-driven swash generated by CASE 7 is chosen as an example for analysis. The different terms in equation (10) are quantified directly from the numerical model at one swash-zone along-slope location (i.e., $x_C=3.0$ m). Figure 15 shows the temporal evolution of each term at two different elevations located near the bed ($z_C=4.5$ mm) and 27 mm above the bed. The local acceleration (III) is not

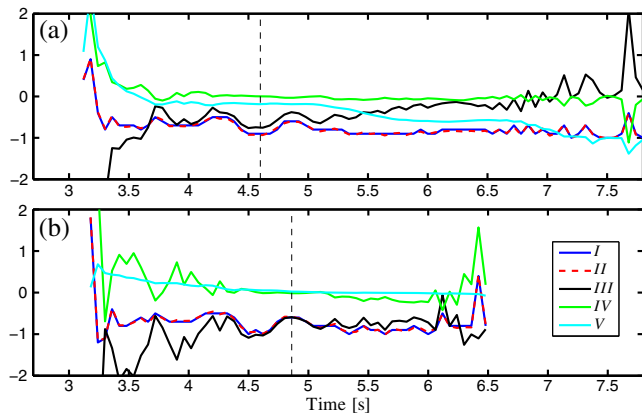


Figure 15. Along-slope momentum balance inside the swash zone ($x_C = 3$ m) at (a) $z_C = 3$ mm and (b) $z_C = 27$ mm for CASE 7. The vertical lines represent the instant when flow reversal occurs.

a good proxy of the total horizontal force (I) during bore arrival irrespective of the elevation in the water column consistent with *Puleo et al.* [2007]. At the near-bed location (Figure 15a), the total fluid stress, i.e., sum of viscous and turbulent stress (V) is the most important term and highly controls the total force evolution (I) along the whole swash cycle.

[35] The high turbulence level during the early stage of the swash cycle is related to the bore-generated turbulence. Subsequently, the turbulence level decreases near flow reversal and then increases during the backwash phase. The latter increase is related to bed-generated turbulence [Sou et al., 2010]. Therefore, at a higher elevations in the water column (i.e., $z_C = 27$ mm), the fluid shear stress (Reynolds + viscous) term is only important during bore arrival and remains small during the rest of the swash cycle. On the other hand, the advection terms (IV) show an opposite trend, increasing in relative importance with elevation. The advection acts against local acceleration (III) during bore arrival and is negligible during the backwash phase near the bed. Moreover, local acceleration depends on the distance from the bed and only increases its correlation with the total force higher in the water column during near flow reversal phase when the other terms are small. It is important to point out that the total force does not show a strong dependence on the elevation in the water column and presents the same temporal evolution independent of the vertical location during the uprush phase (I in Figures 15a–15b) consistent with a hydrostatic pressure distribution. For completeness, the temporal evolution of the summation of all terms in the RHS (II) is plotted as a check of the close balance.

5. Conclusion

[36] Swash-zone hydrodynamics were investigated using a numerical model based on the RANS equations. The numerical model was validated for velocity, runup distance, turbulence intensity, and bed shear stresses with dam-break-driven laboratory swash data. Subsequently, the numerical model was employed to investigate the influence of foreshore characteristics (slope and roughness) on swash-zone hydrodynamics and bed shear stresses. Numerical results suggest that the swash-zone boundary layer thickness essentially vanishes

through flow reversal and increases during backwash until the boundary layer approaches the thinning water surface and the thickness is constrained by backwash depth. Determining the boundary layer length scale during the uprush is a challenge due to existence of both bed shear stress and bore-inertia-driven processes and thus warrants further investigation.

[37] Results revealed that large spatial gradients in bed shear stress can occur in the swash zone. The maximum bed shear stress occurs in the seaward swash region and is always associated with the bore arrival regardless of slope or roughness. The bed shear stress peak moves landward with an increase in foreshore slope and/or bed roughness. The ratio between maximum uprush and maximum backwash bed shear stress is 2–5, (consistent with [e.g., Barnes et al., 2009]). Furthermore, the average tangential force per unit area supplied to the foreshore during the swash event is offshore directed for all cases except in the mild-slope foreshore slope (1:25). Increasing beach slope and bed roughness enhanced the offshore-directed overall mean stress magnitude. Friction coefficient estimates, based on the near-bed velocity gradients and the quadratic drag law, yielded mean values in the range from 3×10^{-3} to 5×10^{-1} , (consistent with field and laboratory observations [e.g., Cowen et al., 2003; Hughes, 1995; Puleo and Holland, 2001; Raubenheimer et al., 2004]) with variations depending on the vertical and cross-slope location where velocity is extracted for the friction coefficient calculation. Friction estimates based on near-bed velocity results in an order of magnitude difference with respect to estimating friction using depth-averaged, mid-water depth, and near-surface velocity. The dependence on the vertical elevation of the velocity used in the friction coefficient computation may partially explain variability in the values reported in the literature.

[38] The momentum balance inside the swash zone is dominated by turbulent and advective transport of momentum during the early and final stage of the swash cycle depending on the elevation. Turbulence is highly correlated with the total force at near-bed elevations, whereas advection becomes important near the surface. The temporal evolution of the total force does not show such dependence consistent with a hydrostatic pressure distribution inside the swash zone. These findings suggest that using an acceleration-enhanced sediment transport formulation may not improve sediment transport predictions in this region.

[39] **Acknowledgments.** This work was supported by the National Council of Science and Technology of Mexico (CB-167692 and M0023-08-06-106400), UNAM (Instituto de Ingenieria Proyecto Interno A2 and DGAPA UNAM PAPIIT IB102012-2), the National Science Foundation CAREER Award (OCE-0845004), and the University of Delaware. Tom Baldock and two anonymous reviewers are thanked for helping to improve the manuscript. We thank one anonymous reviewer for his/her suggestion to investigate flow vorticity during uprush as a possible way to determine the applicability of the log-law model during that phase of the swash cycle.

References

- Aagaard, T., and M. G. Hughes (2006), Sediment suspension and turbulence in the swash zone of dissipative beaches, *Mar. Geol.*, 228(1–4), 117–135, doi:10.1016/j.margeo.2006.01.003.
- Bagnold, R. A. (1963), *Mechanics of marine sedimentation*, in *The Sea*, edited by M. N. Hill, Wiley-Interscience, New York.
- Bailard, J. A. (1981), An energetic total load sediment transport model for a plane sloping beach, *J. Geophys. Res.*, 86(C11), 938–954.

- Baldock, T., and M. Hughes (2006), Field observations of instantaneous water slopes and horizontal pressure gradients in the swash-zone, *Cont. Shelf Res.*, 26(5), 574–588, doi:10.1016/j.csr.2006.02.003.
- Barnes, M. P., and T. E. Baldock (2010), A Lagrangian model for boundary layer growth and bed shear stress in the swash zone, *Coastal Eng.*, 57(4), 385–396, doi:DOI: 10.1016/j.coastaleng.2009.11.009.
- Barnes, M. P., T. O'Donoghue, J. M. Alsina, and T. E. Baldock (2009), Direct bed shear stress measurements in bore-driven swash, *Coastal Eng.*, 56(8), 853–867, doi:DOI: 10.1016/j.coastaleng.2009.04.004.
- Bowen, A. J. (1980), Simple models of nearshore sedimentation; beach profiles and longshore bars, in *The Coastline of Canada*, edited by S. B. McCann, Geological Survey of Canada, Ottawa.
- Briganti, R., N. Dodd, D. Pokrajac, and T. O'Donoghue (2011), Non linear shallow water modelling of bore-driven swash: Description of the bottom boundary layer, *Coastal Eng.*, 58(6), 463–477, doi:DOI: 10.1016/j.coastaleng.2011.01.004.
- Brocchini, M., and T. E. Baldock (2008), Recent advances in modeling swash zone dynamics: Influence of surf-swash interaction on nearshore hydrodynamics and morphodynamics, *Rev. Geophys.*, 46(RG3003).
- Butt, T., P. Russell, J. A. Puleo, and G. Masselink (2005), The application of bagnold-type sediment transport models in the swash zone, *J. Coastal Res.*, 21, 887–8.
- Chorin, A. J. (1968), Numerical solution of the Navier–Stokes equations, *Math. Comput.*, 22, 745–762.
- Conley, D. C., and J. G. Griffin (2004), Direct measurements of bed stress under swash in the field, *J. Geophys. Res.*, 109(3), C03050, 1–12.
- Cowen, E. A., I. M. Sou, P. L.-F. Liu, and B. Raubenheimer (2003), Particle image velocimetry measurements within laboratory-generated swash zone, *J. Eng. Mech.*, 129, 1119–1129.
- Cox, D. T., W. Hobensack, and A. Sukumaran (2000), Bottom stress in the inner surf and swash zone, in *Coastal Engineering 2000 - Proceedings of the 27th International Conference on Coastal Engineering, ICCE 2000*, vol. 276, pp. 108–119.
- Drake, T. G., and J. Calantoni (2001), Discrete particle model for sheet flow sediment transport in the nearshore, *J. Geophys. Res.*, 106(C9), 19,859–19,868.
- Foster, D., A. Bowen, R. Holman, and P. Natoo (2006), Field evidence of pressure gradient induced incipient motion, *J. Geophys. Res.*, 111, C05004, doi:10.1029/2004JC002863.
- Guard, P., and T. Baldock (2007), The influence of seaward boundary conditions on swash zone hydrodynamics, *Coastal Eng.*, 54(4), 321–331, doi:10.1016/j.coastaleng.2006.10.004.
- Hirt, C. W., and B. D. Nichols (1990), Volume of fluid (VOF) method for dynamics of free boundaries, *J. Comput. Phys.*, 39, 201–225.
- Hsu, T.-J., S. Elgar, and R. T. Guza (2006), Wave-induced sediment transport and onshore sandbar migration, *Coastal Eng.*, 53, 817–824.
- Hughes, M. G. (1995), Friction factors for wave uprush, *J. Coastal Res.*, 11(4), 1089–1098.
- Hughes, M. G., and T. E. Baldock (2004), Eulerian flow velocities in the swash zone: Field data and model predictions, *J. Geophys. Res. C: Oceans*, 109(8), C08009, 1–11.
- Hughes, M. G., G. Masselink, and R. W. Brander (1997a), Flow velocity and sediment transport in the swash zone of a steep beach, *Mar. Geol.*, 138(1–2), 91–103, doi:10.1016/S0025-3227(97)00014-5.
- Hughes, M. G., G. M. D. Hanslow, and D. Mitchell (1997b), Toward a better understanding of swash zone sediment transport, in *Coastal Dynamics - Proceedings of the International Conference*, pp. 804–813.
- Jackson, N. L., G. Masselink, and K. F. Nordstrom (2004), The role of bore collapse and local shear stresses on the spatial distribution of sediment load in the uprush of an intermediate-state beach, *Mar. Geol.*, 203(1–2), 109–118, doi:10.1016/S0025-3227(03)00328-1.
- Justesen, P. (1988), Prediction of turbulent oscillatory flow over rough beds, *Coastal Eng.*, 12(3), 257–284, doi:DOI: 10.1016/0378-3839(88)90008-7.
- Kirkz, M. S. (1981), A theoretical study of plunging breakers and their run-up, *Coastal Eng.*, 5(0), 353–370, doi:10.1016/0378-3839(81)90023-5.
- Kobayashi, N., G. S. Desilva, and K. D. Watson (1989), Wave transformation and swash oscillation on gentle and steep slopes, *J. Geophys. Res.*, 94(C1), 951–966.
- Kothe, D. B., R. C. Mjølness, and M. D. Torrey (1991), RIPPLE: A computer program for incompressible flows with free surface, *Tech. Rep. Rep.96-5*, Los Alamos National Laboratory.
- Lara, J. L., I. J. Losada, and P. L. F. Liu (2006), Breaking waves over a mild gravel slope: experimental and numerical analysis, *J. Geophys. Res.*, 111(C11019), doi:10.1029/2005JC003374.
- Lin, P., and P. L.-F. Liu (1998), A numerical study of breaking waves in the surf zone, *J. Fluid Mech.*, 359, 239–264.
- Liu, P. L.-F., and P. Lin (1997), A numerical model for breaking waves: The volume of fluid method, *Tech. Rep. Rep. CACR-97-02*, Cent. for Appl. Coastal Res., Univ. of Delaware, Newark.
- Losada, I. J., J. L. Lara, R. Guanache, and J. M. González-Ondina (2008), Numerical analysis of wave overtopping of high mound breakwaters, *Coastal Eng.*, 55, 47–62.
- Madsen, O. (1974), Stability of a sand bed under breaking waves, in *Proc. 14th Int. Conf. Coastal Eng.*, pp. 776–794.
- Masselink, G., and M. G. Hughes (1998), Field investigation of sediment transport in the swash zone, *Cont. Shelf Res.*, 18(10), 1179–1199.
- Masselink, G., and J. A. Puleo (2006), Swash-zone morphodynamics, *Cont. Shelf Res.*, 26(5), 661–680, doi:10.1016/j.csr.2006.01.015.
- Masselink, G., D. Evans, M. G. Hughes, and P. Russell (2005), Suspended sediment transport in the swash zone of a dissipative beach, *Mar. Geol.*, 216(3), 169–189, doi:10.1016/j.margeo.2005.02.017.
- Nielsen, P. (1992), *Coastal Bottom Boundary Layers and Sediment Transport, Advanced Series on Ocean Engineering*, vol. 24, 324 pp., World Scientific, River Edge, NJ.
- O'Donoghue, T., D. Pokrajac, and L. Hondebrink (2010), Laboratory and numerical study of dambreak-generated swash on impermeable slopes, *Coastal Eng.*, 57(5), 513–530, doi:10.1016/j.coastaleng.2009.12.007.
- Pedrozo-Acuna, A., A. Torres-Freyermuth, Q. Zou, T.-J. Hsu, and D. E. Reeve (2010), Diagnostic investigation of impulsive pressures induced by plunging breakers impinging on gravel beaches, *Coastal Eng.*, 57(3), 252–266, doi:DOI: 10.1016/j.coastaleng.2009.09.010.
- Pedrozo-Acuna, A., A. R. de Alegria-Arzaburu, A. Torres-Freyermuth, E. Mendoza, and R. Silva (2011), Laboratory investigation of pressure gradients induced by plunging breakers, *Coastal Eng.*, 58(8), 722–738, doi:10.1016/j.coastaleng.2011.03.013.
- Petti, M., and S. Longo (2001), Turbulence experiments in the swash zone, *Coastal Eng.*, 43(1), 1–24, doi:10.1016/S0378-3839(00)00068-5.
- Puleo, J. A., and K. Holland (2001), Estimating swash zone friction coefficients on a sandy beach, *Coastal Eng.*, 43(1), 25–40, doi:10.1016/S0378-3839(01)00004-7.
- Puleo, J. A., R. A. Beach, R. A. Holman, and J. S. Allen (2000), Swash zone sediment suspension and transport and the importance of bore-generated turbulence, *J. Geophys. Res.*, 105, C07007.
- Puleo, J. A., K. T. Holland, N. Plant, D. N. Slinn, and D. M. Hanes (2003), Fluid acceleration effects on suspended sediment transport in the swash zone, *J. Geophys. Res.*, 108, 3350, doi:10.1029/2003JC001943.
- Puleo, J. A., A. Farhadzadeh, and N. Kobayashi (2007), Numerical simulation of swash zone fluid accelerations, *J. Geophys. Res.*, 112, C07007, doi:10.1029/2006JC004084.
- Puleo, J. A., T. M. Lanckriet, and P. Wang (2012), Near bed cross-shore velocity profiles, bed shear stress and friction on the foreshore of a microtidal beach, *Coastal Eng.*, 68(10), 6–16.
- Raubenheimer, B. (2002), Observations and predictions of fluid velocities in the surf and swash zones, *J. Geophys. Res.*, 107, 3190, doi:10.1029/2001JC001264.
- Raubenheimer, B., S. Elgar, and R. T. Guza (2004), Observations of swash zone velocities: A note on friction coefficients, *J. Geophys. Res.*, 109, C01027, doi:10.1029/2001JC001264.
- Rodi, W. (1993), *Turbulence Models and Their Application in Hydraulics - A State-of-the-Art Review*, Int. Assoc. for Hydraul. Res., Delft, Netherlands.
- Shen, M. C., and R. E. Meyer (1963), Climb of a bore on a beach: Part 3, run-up, *J. Fluid Mech.*, 16(8), 113–125.
- Sleath, J. (1999), Conditions for plug formation in oscillatory flow, *Cont. Shelf Res.*, 19(13), 1643–1664.
- Sou, I., E. Cowen, and P.-F. Liu (2010), Evolution of the turbulence structure in the surf and swash zones, *J. Fluid Mech.*, 644, 193–216.
- Sou, I. M., and H. Yeh (2011), Laboratory study of the cross-shore flow structure in the surf and swash zones, *J. Geophys. Res.*, 116(C03002), doi:10.1029/2010JC006700.
- Sumer, B., M. Sen, I. Karagali, B. Ceren, J. Fredse, M. Sottile, L. Zilioli, and D. Fuhrman (2011), Flow and sediment transport induced by a plunging solitary wave, *J. Geophys. Res.*, 116(C1), doi:10.1029/2010JC006435.
- Torres-Freyermuth, A., and T.-J. Hsu (2010), On the dynamics of wave-mud interaction: A numerical study, *J. Geophys. Res.*, 115(C07014), doi:10.1029/2009JC005552.
- Torres-Freyermuth, A., I. J. Losada, and J. L. Lara (2007), Modeling of surf zone processes on a natural beach using Reynolds-Averaged Navier–Stokes equations, *J. Geophys. Res.*, 112(L05601), doi:10.1029/2006JC004050.
- Torres-Freyermuth, A., J. L. Lara, and I. J. Losada (2010), Numerical modelling of short- and long-wave transformation on a barred beach, *Coastal Eng.*, 57(3), 317–330, doi:DOI: 10.1016/j.coastaleng.2009.10.013.
- Wilcox, D. C. (2000), *Turbulence Modeling for CFD*, DCW Industries, Inc., La Canada, CA.
- Yeh, H. (1991), Vorticity-generation mechanisms in bores, *Proc. R. Soc. A.*, 432, 215–231.
- Yen, B. C. (2002), Open channel flow resistance, *J. Hydraul. Eng.*, 128(1), 20–39.
- Yu, X., T.-J. Hsu, and D. Hanes (2010), Sediment transport under wave groups: Relative importance between nonlinear waveness and nonlinear boundary layer streaming, *J. Geophys. Res.*, 115(C02013), doi:10.1029/2009JC005348.
- Zhang, Q., and P. L.-F. Liu (2008), A numerical study of swash flows generated by bores, *Coastal Eng.*, 55(12), 1113–1134, doi:10.1016/j.coastaleng.2008.04.010.